J. of Thermal Science Vol.6, No.4

Effect of Nonequilibrium Condensation of Moist Air on the Boundary Layer in a Supersonic Nozzle

Shigeru Matsuo, Toshiaki Setoguchi

Department of Mechanical Engineering, Saga University, 1, Honjo–machi, Saga–shi, Saga, 840, Japan

Shen Yu

Institute of Engineering Thermophysics, Chinese Academy of Sciences, P.O. Box 2706, Beijing 100080, China

Kazuyasu Matsuo

Graduate School of Engineering Sciences, Kyushu University, 6, Kasuga–koen, Kasuga–shi, Fukuoka, 816, Japan

When condensation occurs in supersonic flow fields, the flow is affected by the latent heat released. In the present study, Navier–Stokes equations were solved numerically using a 3rd–order MUSCL type TVD finite–difference scheme with a second–order fractional–step for time integration. Baldwin–Lomax model, that is the algebraic model, called the zero equation model was used in the computations. The effects of initial conditions (initial degree of supersaturation and total temperature in the reservoir) on condensing flow of moist air in a supersonic circular half nozzle were investigated. In this case, the effect of condensation on the boundary layer was also discussed in detail. As a result, the simulated flow fields were compared with experimental data in good agreement, and the velocity and temperature profiles were largely changed by condensation.

Keywords: numerical simulation, compressible flow, condensation, boundary layer, moist air.

INTRODUCTION

Many studies[1−13] on the condensation shock wave occurring in the case of the rapid expansion of moist air or steam in a supersonic nozzle have been performed, and the characteristics of condensation shock wave have nearly been clarified. A condensation shock wave also occurs in the blade passage in a steam turbine[14,15]. Such a condensation shock wave that interacts with the boundary layer on the surface of the turbine blade, affects the flow in the blade passage in a steam turbine. However, the flow in the blade passage with the condensation shock wave is not yet understood satisfactorily[16,17].

For condensation phenomena of moist air in the supersonic nozzle, Schnerr et al.[18] conducted the simulation using a combination of analytical and numerical methods, and clarified the effect of condensation on the boundary layer. Yamamoto et al.[19] and Schnerr et al.[12] investigated the effect of condensation on shock wave on surface wing. However, they did not refer to the effect of condensation on boundary layer. Setoguchi et al.[20] showed the effect of condensation on the thickness of boundary layer experimentally. Furthermore, in order to confirm the usefulness of experimental results, Setoguchi et al. solved Navier–Stokes equations without a turbulence model in the computa-

Received, 1997.

Nomenclature

C_f	skin friction coefficient
C_p	specific heat at constant pressure
I	nucleation rate (1/m^{3}s)
L	latent heat of condensation[22]
M	molecular mass
N_A	Avogadro's number
P_r	Prandtl number of mixture
R_e	Reynolds number
R	radius of nozzle
$\Re$	universal gas constant(=8314.41 (J/kmol· K))
S	supersaturation
T	temperature
c	frozen sound speed[23]
e_m	total energy per unit volume of mixture
g	condensate mass fraction
k	Boltzmann constant (=1.380622^{-23} (J/K))
l_0	characteristic length
m	mass
p	pressure
p_∞	saturated vapour pressure[24]
r	radius of droplet
r_c	critical radius of nuclei
t	time
u, v	velocity component in Cartesian coordinate
x, y	Cartesian coordinate
Γ	accommodation coefficient for nucleation
γ	ratio of specific heats of mixture
δ^*	displacement thickness
ζ	coefficient of surface tension
κ	Karman constant
μ	kinetic viscosity
ν	kinematic viscosity
ξ, η	generalized coordinate system
ξ_c	condensation coefficient
ρ	density
σ_∞	surface tension in flat surface
τ	shear stress
	Subscripts
0	condition in the reservoir section
W	wall
f	frozen
a	air
l	liquid
m	mixture
v	vapour
∞	main stream

tion and showed reduction of the displacement thickness of boundary layer in case with condensation. Thus, in the previous study, the effect of condensing flow on boundary layer has not yet been clarified satisfactorily for the case of high relative humidity with strong condensation shock wave that is observed in the blade passages of a steam turbine and so on. Therefore, it is important to investigate the interaction phenomena of the boundary layer and condensing flow with strong condensation shock.

In the present study, Navier–Stokes equations were solved numerically using a 3rd–order MUSCL type TVD finite–difference scheme with a second–order fractional–step for time integration. Baldwin–Lomax model[21], that is the algebraic model, called the zero equation model was used in the computations. The effects of initial conditions (degree of supersaturation S_0 and total temperature T_0 in the reservoir) on condensing flow of moist air with a condensation shock wave in a supersonic circular half nozzle were investigated together with the effect of the condensation on the boundary layer.

NUMERICAL PROCEDURES

Governing Equations

Assumptions using in the present calculation of the two phase flow are as follows:

1. No velocity slip exists between condensate particles and gas mixture.
2. No temperature difference exists between condensate particles and gas mixture.
3. Effect of the condensate particles on pressure is neglected.

The governing equations under consideration are the unsteady two–dimensional compressible Navier–Stokes equations and droplet growth equation[25] written in the Cartesian coordinate system (x, y). To obtain the normalized conservation equations, all variables are non–dimensionalized as follows:

$$\begin{array}{lll} u^* = \overline{u}/\overline{c}_0 & v^* = \overline{v}/\overline{c}_0 & t^* = \overline{t}/(\overline{L}/\overline{c}_0) \\ x^* = \overline{x}/\overline{L} & y^* = \overline{y}/\overline{L} & \rho^* = \overline{\rho}/\overline{\rho}_0 \\ T^* = \overline{T}/\overline{T}_0 & p^* = \overline{p}/(\gamma_m \overline{p}_0) & \mu^* = \overline{\mu}/\overline{\mu}_0 \\ e_m^* = \overline{e}_m/(\overline{\rho}_0 \overline{c}_0^2) & & \end{array}$$

where overbar notation indicates dimensional quantity. The governing equations that superscript $*$ is omitted, can be written as

$$\frac{\partial U}{\partial t} + \frac{\partial E}{\partial x} + \frac{\partial F}{\partial y} = \frac{1}{Re}\left(\frac{\partial R}{\partial x} + \frac{\partial S}{\partial y}\right) + Q \quad (1)$$

where

$$U=\begin{bmatrix}\rho_m\\ \rho_m u\\ \rho_m v\\ e_m\\ \rho_m g\\ \rho_m D_1\\ \rho_m D_2\\ \rho_m D_3\end{bmatrix},\quad E=\begin{bmatrix}\rho_m u\\ \rho_m u^2+p\\ \rho_m uv\\ u(e_m+p)\\ \rho_m ug\\ \rho_m uD_1\\ \rho_m uD_2\\ \rho_m uD_3\end{bmatrix},$$

$$F=\begin{bmatrix}\rho_m v\\ \rho_m uv\\ \rho_m v^2+p\\ v(e_m+p)\\ \rho_m vg\\ \rho_m vD_1\\ \rho_m vD_2\\ \rho_m vD_3\end{bmatrix}\quad R=\begin{bmatrix}0\\ \tau_{xx}\\ \tau_{xy}\\ \alpha\\ 0\\ 0\\ 0\\ 0\end{bmatrix},$$

$$S=\begin{bmatrix}0\\ \tau_{xy}\\ \tau_{yy}\\ \beta\\ 0\\ 0\\ 0\\ 0\end{bmatrix},\quad Q=\begin{bmatrix}0\\ 0\\ 0\\ 0\\ \rho_m\dot{g}\\ \rho_m\dot{D}_1\\ \rho_m\dot{D}_2\\ \rho_m\dot{D}_3\end{bmatrix}$$

In these equations,

$$e_m=\rho_m C_{p0}T-p+\frac{1}{2}\rho_m(u^2+v^2)-\rho_m gL$$

$$\alpha=u\tau_{xx}+v\tau_{yx}+\frac{\mu}{(\gamma-1)P_r}\frac{\partial T}{\partial x}$$

$$\beta=u\tau_{xy}+v\tau_{yy}+\frac{\mu}{(\gamma-1)P_r}\frac{\partial T}{\partial y}$$

$$p=\rho_m(1-g)\Re T$$

$$L=2.353\times10^6-5.72\times10^4(\ln p-10)$$
$$-4.60\times10^3(\ln p-10)^2\quad (J/kg)$$

τ_{xx}, τ_{xy}, τ_{yx} and τ_{yy} are components of viscous shear stress. $\dot{g}$, $\dot{D}_1$, $\dot{D}_2$ and $\dot{D}_3$ are indicated as follows:

$$\dot{g}=\frac{dg}{dt}=\frac{\rho_c}{\rho_m}\left\{\frac{4\pi}{3}r_c^3 I_F+\rho_m D_1\frac{dr}{dt}\right\}$$

$$\dot{D}_1=\frac{dD_1}{dt}=\frac{4\pi r_c^2 I_F}{\rho_m}+D_2\frac{dr}{dt}$$

$$\dot{D}_2=\frac{dD_2}{dt}=\frac{8\pi r_c I_F}{\rho_m}+D_3\frac{dr}{dt}$$

$$\dot{D}_3=\frac{dD_3}{dt}=\frac{8\pi I_F}{\rho_m}$$

Using dimensional quantities, these equations may be expressed as follows:

$$\dot{g}=\frac{\bar{l}}{\bar{c}_0}\times\frac{dg}{d\bar{t}}$$

$$\dot{D}_1=\frac{\bar{l}^2}{\bar{c}_0}\times\frac{d\overline{D}_1}{d\bar{t}}$$

$$\dot{D}_2=\frac{\bar{l}^3}{\bar{c}_0}\times\frac{d\overline{D}_2}{d\bar{t}}$$

$$\dot{D}_3=\frac{\bar{l}^4}{\bar{c}_0}\times\frac{d\overline{D}_3}{d\bar{t}}$$

Nucleation rate I_F[26], critical radius of the nuclei r_c and radius growth rate $\dot{r}$ are

$$I_F=\Gamma\cdot I, \tag{2}$$

$$I=\frac{1}{\rho_l}\left(\frac{p_v}{\mathrm{k}T}\right)^2\sqrt{\frac{2\sigma M_v}{N_A\pi}}\exp\left\{\frac{-4\pi\sigma r_c^2}{3kT}\right\}, \tag{3}$$

$$r_c=\frac{2\sigma}{\rho_l\Re T\ln(p_v/p_\infty)}, \tag{4}$$

and

$$\dot{r}=\frac{\xi_c}{\rho_l}\frac{p_\infty}{\sqrt{2\pi\Re T}}\left(\frac{p_v}{p_\infty}-1\right) \tag{5}$$

respectively.
where

$$p_\infty=10^{(-A/T+B)}\times101325(Pa)$$

$$\begin{cases}A=2263,\quad B=6.064\quad (T=273\sim395\mathrm{K})\\ A=2672,\quad B=7.582\quad (T=175\sim273\mathrm{K})\end{cases}$$

$$\rho_l=1000\quad (\mathrm{kg/m^3})$$

Γ[27] and ξ_c[28,29] are accommodation coefficient for nucleation and condensation coefficient, respectively. Surface tension σ[25,27,30] is given by using the surface tension of an infinite flat-film σ_∞ and the coefficient of surface tension[31,32,33] ζ as follows:

$$\sigma=\zeta\sigma_\infty$$

$$\sigma_\infty=(128-0.192T)\times10^{-3}(\mathrm{N/m})$$

In calculation, values chosen for Γ, ξ_c and ζ[36] are

$$\Gamma=10^6,\ \xi_c=0.9,\ \zeta=1.29$$

Calculation Procedures

The unsteady two-dimensional compressible Euler equations are written in the generalized coordinate system as follows:

$$\frac{\partial\hat{\mathbf{U}}}{\partial t}+\frac{\partial\hat{\mathbf{E}}}{\partial\xi}+\frac{\partial\hat{\mathbf{F}}}{\partial\eta}=\frac{1}{R_e}\left(\frac{\partial\hat{\mathbf{R}}}{\partial\xi}+\frac{\partial\hat{\mathbf{S}}}{\partial\eta}\right)+\hat{\mathbf{Q}} \tag{6}$$

where

$$\hat{\mathbf{U}}=\mathbf{J}\mathbf{U},\hat{\mathbf{E}}=\mathbf{J}(\xi_x\mathbf{E}+\xi_y\mathbf{F}),\hat{\mathbf{F}}=\mathbf{J}(\eta_x\mathbf{E}+\eta_y\mathbf{F}),$$

$$\hat{\mathbf{R}}=\mathbf{J}(\xi_x\mathbf{R}+\xi_y\mathbf{S}),\hat{\mathbf{S}}=\mathbf{J}(\eta_x\mathbf{R}+\eta_y\mathbf{S}),\hat{\mathbf{Q}}=\mathbf{J}\mathbf{Q} \tag{7}$$

$$\mathbf{J}^{-1}=\xi_x\eta_y-\xi_y\eta_x$$

In order to solve the set of above equations, 3rd-order MUSCL type TVD finite-difference scheme with a second-order fractional-step for time integration are adopted to the flow equations and the droplet growth equation and a second-order centered difference scheme is used for viscous terms. The discrete equation of 3rd-order MUSCL type TVD scheme can be approximated as

$$\begin{aligned}\hat{\mathbf{U}}^{n+1}_{i,j}=\hat{\mathbf{U}}^{n}_{i,j}&-\lambda^{\xi}(\hat{\mathbf{E}}^{n}_{i+1/2,j})\\&-\lambda^{\eta}(\hat{\mathbf{F}}^{n}_{i,j+1/2}-\hat{\mathbf{F}}^{n}_{i,j-1/2})\\&+(\lambda^{\xi}(\hat{\mathbf{R}}^{n}_{i+1/2,j}-\hat{\mathbf{R}}^{n}_{i-1/2,j})\\&+(\lambda^{\eta}(\hat{\mathbf{S}}^{n}_{i,j+1/2}-\hat{\mathbf{S}}^{n}_{i,j-1/2}))/Re+\Delta t\hat{\mathbf{Q}}^{n}_{i,j}\end{aligned}$$

where

$$\lambda^{\xi}=\Delta t/\Delta\xi,\quad \lambda^{\eta}=\Delta t/\Delta\eta$$

$\Delta t, \Delta\xi$ and $\Delta\eta$ indicate the time step, the mesh spacing in the ξ,η directions, respectively.

The numerical flux $\hat{\mathbf{E}}_{i+\frac{1}{2}}$ that notation for j is omitted for simplicity, can be

$$\begin{aligned}\hat{\mathbf{E}}_{i+\frac{1}{2}}=\frac{1}{2}\{&(y_\eta)_{i+1/2}[\mathbf{E}(\mathbf{U}^R_{i+1/2})+\mathbf{E}(\mathbf{U}^L_{i+1/2})]\\&-(x_\eta)_{i+1/2}[\mathbf{F}(\mathbf{U}^R_{i+1/2})+\mathbf{F}(\mathbf{U}^L_{i+1/2})]\\&+\hat{T}_{i+1/2}\hat{\mathbf{\Phi}}_{i+1/2}\mathbf{J}_{i+1/2}\}\end{aligned}$$

Terms for $\hat{\mathbf{F}}^n_{i,j+1/2}$ have a similar form also.

Matrices $\hat{T}$ and $\hat{\mathbf{\Phi}}$ are expressed using eigenvectors and eigenvalues[34]. The values of mesh points $(i+1/2,j)$ for matrix are given by arithmetic average of values in mesh points (i,j) and $(i+1,j)$

The numerical fluxes of $\mathbf{E}(\mathbf{U}^R_{i+\frac{1}{2}})$ and $\mathbf{E}(\mathbf{U}^L_{i+\frac{1}{2}})$ are ones evaluated by $\mathbf{U}^R_{i+\frac{1}{2}}$ and $\mathbf{U}^L_{i+\frac{1}{2}}$ as follows:

$$\mathbf{U}^R_{i+1/2}=\mathbf{U}_{i+1,j}-\frac{1}{4}[(1-\varepsilon)\Delta^{*}_{i+3/2}+(1+\varepsilon)\Delta^{**}_{i+1/2}]$$

$$\mathbf{U}^L_{i+1/2}=\mathbf{U}_{i,j}+\frac{1}{4}[(1-\varepsilon)\Delta^{**}_{i-1/2}+(1+\varepsilon)\Delta^{*}_{i+1/2}]$$

where

$$\Delta^{*}=\mathrm{minmod}(\Delta_{i+1/2},\overline{\beta}\Delta_{i-1/2})$$

$$\Delta^{**}=\mathrm{minmod}(\Delta_{i+1/2},\overline{\beta}\Delta_{i+3/2})$$

$$\mathrm{minmod}(x,\overline{\beta}_y)=\mathrm{sgn}(x)\cdot\max\{0,\min[|x|,\mathrm{sgn}(x)\cdot\overline{\beta}y]\}$$

$$\Delta_{i+1/2}=\mathbf{U}_{i+1,j}-\mathbf{U}_{i,j}$$

$$\overline{\beta}=\frac{3-\varepsilon}{1-\varepsilon}$$

The spatial order of accuracy is determined by the value of ε. In the present calculation, $\varepsilon=\frac{1}{3}(\overline{\beta}=4)$ is used to obtain the spatial 3rd order of accuracy.

In calculation, the two-dimensional flux Jacobian matrices in generalized coordinates for $\hat{\Psi}_\xi=\partial\hat{\mathbf{E}}/\partial\hat{\mathbf{U}}$ and $\hat{\Psi}_\eta=\partial\hat{\mathbf{F}}/\partial\hat{\mathbf{U}}$ are as follows:

$$\hat{\Psi}_\xi \quad \text{or} \quad \hat{\Psi}_\eta=$$

$$\left[\begin{array}{cccccccc}
0 & k_x & k_y & 0 & 0 & 0 & 0 & 0\\
-u\theta+k_x\phi & \theta-(G-1)k_xu & k_yu-Gk_xv & k_xG & k_x(G-\rho_mK) & 0 & 0 & 0\\
-v\theta+k_y\phi & k_xv-Gk_yu & \theta-(G-1)k_yv & k_yG & k_y(G-\rho_mK) & 0 & 0 & 0\\
\theta(\phi-\delta) & k_x\delta-Gu\theta & k_y\delta-Gv\theta & (G+1)\theta & \theta(GL-\rho_mK) & 0 & 0 & 0\\
-g\theta & k_xg & k_yg & 0 & \theta & 0 & 0 & 0\\
-D_1\theta & k_xD_1 & k_yD_1 & 0 & 0 & \theta & 0 & 0\\
-D_2\theta & k_xD_2 & k_yD_2 & 0 & 0 & 0 & \theta & 0\\
-D_3\theta & k_xD_3 & k_yD_3 & 0 & 0 & 0 & 0 & \theta
\end{array}\right]$$

$$G=(1-g\frac{M_m}{M_v})(\frac{1}{\gamma_m-1}+g\frac{M_m}{M_v})^{-1}$$

$$K=Z\{e_m-\frac{1}{2}\rho_m(u^2+v^2)+\rho_mgL\}$$

$$Z=\left(\left(\frac{1}{\gamma-1}+1\right)\frac{M_m}{M_v}\right)\left(\rho_m\left(\frac{1}{\gamma_m-1}+g\frac{M_m}{M_v}\right)\right)^{-2}$$

$$\delta=\psi+(G+1)\frac{e_m}{\rho_m}$$

$$\theta=k_xu+k_yv$$

$$\phi = GgL + \frac{1}{2}G(u^2 + v^2)$$

$$\psi = GgL - \frac{1}{2}G(u^2 + v^2)$$

with $k = \xi$ or η for $\hat{\Psi}_\xi$ or $\hat{\Psi}_\eta$, respectively.

The flux Jacobian matrices have real eigenvalues and a complete set of eigenvectors.

The similarity transforms[35] are as follows:

$$\hat{\Psi}_\xi = \hat{T}_\xi \hat{\Lambda}_\xi \hat{T}_\xi^{-1}, \quad \hat{\Psi}_\eta = \hat{T}_\eta \hat{\Lambda}_\eta \hat{T}_\eta^{-1}$$

where

$$\hat{\Lambda}_\xi = D[U, U, U + c\sqrt{\xi_x^2 + \xi_y^2}, U - c\sqrt{\xi_x^2 + \xi_y^2}, U, U, U, U] = \begin{bmatrix} U & 0 & 0 & 0 & 0 & 0 & 0 & 0 \\ 0 & U & 0 & 0 & 0 & 0 & 0 & 0 \\ 0 & 0 & U + c\sqrt{\xi_x^2 + \xi_y^2} & 0 & 0 & 0 & 0 & 0 \\ 0 & 0 & 0 & U - c\sqrt{\xi_x^2 + \xi_y^2} & 0 & 0 & 0 & 0 \\ 0 & 0 & 0 & 0 & U & 0 & 0 & 0 \\ 0 & 0 & 0 & 0 & 0 & U & 0 & 0 \\ 0 & 0 & 0 & 0 & 0 & 0 & U & 0 \\ 0 & 0 & 0 & 0 & 0 & 0 & 0 & U \end{bmatrix}$$

$$\hat{\Lambda}_\eta = D[V, V, V + c\sqrt{\eta_x^2 + \eta_y^2}, V - c\sqrt{\eta_x^2 + \eta_y^2}, V, V, V, V] = \begin{bmatrix} V & 0 & 0 & 0 & 0 & 0 & 0 & 0 \\ 0 & V & 0 & 0 & 0 & 0 & 0 & 0 \\ 0 & 0 & V + c\sqrt{\eta_x^2 + \eta_y^2} & 0 & 0 & 0 & 0 & 0 \\ 0 & 0 & 0 & V - c\sqrt{\eta_x^2 + \eta_y^2} & 0 & 0 & 0 & 0 \\ 0 & 0 & 0 & 0 & V & 0 & 0 & 0 \\ 0 & 0 & 0 & 0 & 0 & V & 0 & 0 \\ 0 & 0 & 0 & 0 & 0 & 0 & V & 0 \\ 0 & 0 & 0 & 0 & 0 & 0 & 0 & V \end{bmatrix}$$

$$\hat{T}_k = \begin{bmatrix} 1 & 0 & \beta_1 & \beta_1 & 0 & 0 & 0 & 0 \\ u & \tilde{k}_y \rho_m & \beta_1(u + \tilde{k}_x c) & \beta_1(u - \tilde{k}_x c) & 0 & 0 & 0 & 0 \\ v & -\tilde{k}_x \rho_m & \beta_1(v + \tilde{k}_y c) & \beta_1(v - \tilde{k}_y c) & 0 & 0 & 0 & 0 \\ \frac{\psi}{G} & \rho_m(\tilde{k}_y u - \tilde{k}_x v) & \beta_1(\frac{\psi + c^2}{G} + c\tilde{\theta}) & \beta_1(\frac{\psi + c^2}{G} - c\tilde{\theta}) & \frac{\rho_m(\rho_m K - GL)}{G} & 0 & 0 & 0 \\ g & 0 & g\beta_1 & g\beta_1 \rho_m & 0 & 0 & 0 & \\ D_1 & 0 & D_1\beta_1 & D_1\beta_1 & 0 & \rho_m & 0 & 0 \\ D_2 & 0 & D_2\beta_1 & D_2\beta_1 & 0 & 0 & \rho_m & 0 \\ D_3 & 0 & D_3\beta_1 & D_3\beta_1 & 0 & 0 & 0 & \rho_m \end{bmatrix}$$

$$\hat{T}_k^{-1} = \begin{bmatrix} 1-\phi c^{-2} & Gc^{-2}u & Gc^{-2}v & Gc^{-2} & (\rho_m K - GL)c^{-2} & 0 & 0 & 0 \\ -\rho^{-1}(\tilde{k}_y u - \tilde{k}_x v) & \tilde{k}_y \rho_m^{-1} & -\tilde{k}_x \rho_m^{-1} & 0 & 0 & 0 & 0 & 0 \\ \beta_2(\phi - c\tilde{\theta}) & \beta_2(\tilde{k}_x c - Gu) & \beta_2(\tilde{k}_y c - Gv) & \beta_2 G & -(\rho_m K - GL)\beta_2 & 0 & 0 & 0 \\ \beta_2(\phi + c\tilde{\theta}) & -\beta_2(\tilde{k}_x c + Gu) & -\beta_2(\tilde{k}_y c + Gv) & \beta_2 G & -(\rho_m K - GL)\beta_2 & 0 & 0 & 0 \\ -g\rho_m^{-1} & 0 & 0 & 0 & \rho_m^{-1} & 0 & 0 & 0 \\ -D_1\rho_m^{-1} & 0 & 0 & 0 & 0 & \rho_m^{-1} & 0 & 0 \\ -D_2\rho_m^{-1} & 0 & 0 & 0 & 0 & 0 & \rho_m^{-1} & 0 \\ -D_3\rho_m^{-1} & 0 & 0 & 0 & 0 & 0 & 0 & \rho_m^{-1} \end{bmatrix}$$

$$\beta_1 = \frac{\rho_m}{\sqrt{2}c}, \quad \beta_2 = \frac{1}{\sqrt{2}\rho_m c},$$

$$\tilde{k}_x = \frac{k_x}{\sqrt{k_x^2 + k_y^2}}, \quad \tilde{k}_y = \frac{k_y}{\sqrt{k_x^2 + k_y^2}},$$

$$\tilde{\theta} = \tilde{k}_x u + \tilde{k}_y v, \quad c^2 = (G+1)\frac{p}{\rho_m}$$

$$U = \xi_x u + \xi_y v, \quad V = \eta_x u + \eta_y v$$

U and V are the so-called contravariant velocities along the ξ and η coordinates.

Turbulence Modeling

In this calculation, the boundary layer is considered as turbulent because Reynolds number is in the order of 10^6. An algebraic eddy viscosity model developed by Baldwin-Lomax[21] was used to define the turbulent transport. This model permits the calculation of the turbulent characteristics of the boundary layer by defining a two-layer system. Thus, in stress terms of the laminar Navier–Stokes equations, the molecular coefficient of viscosity μ is replaced by $\mu_l + \mu_t$. μ_l is calculated from Sutherland equation as follows:

$$\frac{\mu_l}{\mu_0} = \left(\frac{T}{T_0}\right)^{3/2} \frac{T_0 + 110.6}{T + 110.6}$$

In the inner region, the eddy viscosity is given by simple mixing length theory by the Prandtl-Van Driest formulation as follows:

$$(\mu_t)_{\text{inner}} = \rho l^2 |\omega| \tag{8}$$

where

$$l = \kappa y \left\{1 - \exp(-\frac{y^+}{A^+})\right\}$$

$$y^+ = \frac{\rho_W u_\tau y}{\mu_W} = \frac{\sqrt{\rho_W \tau_W}}{\mu_W} y \quad \left(u_\tau = \sqrt{\frac{\tau_W}{\rho_W}}\right)$$

Subscript W indicates the wall. u_τ is the friction velocity. $|\omega|$ is the magnitute of the vorticity given by

$$|\omega| = \left|\frac{\partial u}{\partial y} - \frac{\partial v}{\partial x}\right|$$

In the outer region, the eddy viscosity in place of the Clauser formulation is calculated as follows:

$$(\mu_t)_{\text{outer}} = K \cdot C_{\text{CP}} \cdot \rho \cdot F_{\text{WAKE}} \cdot F_{\text{KLEB}}(y) \tag{9}$$

where K is Clauser constant, C_{CP} is an additional constant. F_{WAKE} is defined as the minimum value as follows:

$$F_{\text{WAKE}} = \min\left(y_{\max} F_{\max}, C_{\text{WK}} y_{\max} \frac{U_{\text{DIF}}^2}{F_{\max}}\right)$$

The quantity of $F_{\max}$ are determined from the maximum value of

$$F(y) = y|\omega| \left\{1 - \exp\left(-\frac{y^+}{A^+}\right)\right\}$$

$y_{\max}$ are defined as the value of y at which $F_{\max}$ occurs. The Klebanoff intermittency factor $F_{\text{KLEB}}(y)$ is given by

$$F_{\text{KLEB}}(y) = \left\{1 + 5.5(\frac{C_{\text{KLEB}}}{y_{\max}} y)^6\right\}^{-1}$$

The function U_{DIF} is given as follows:

$$U_{\text{DIF}} = (\sqrt{u^2 + v^2})_{\max} - (\sqrt{u^2 + v^2})_{\min}$$

The constants appearing in the foregoing relations are

$$
\begin{cases}
A^+ & = 26.0 \\
C_{\mathrm{CP}} & = 1.6 \\
C_{\mathrm{KLEB}} & = 0.30 \\
C_{\mathrm{WK}} & = 0.25 \\
K & = 0.0168 \\
\kappa & = 0.4
\end{cases}
$$

Initial and Boundary Conditions

The degree of supersaturation S_0, total temperature T_0 and specific humidity $\omega_0(= m_{v0}/(m_{v0}+m_{a0}))$ in the reservoir used in the present calculation are shown in Table 1. Total pressure in the reservoir is set at p_0=102 kPa. Hereafter each condition will be denoted as Case 1 to 4 respectively in this paper.

Table 1 Initial conditions

	S_0	T_0 [K]	ω_0 [kg/kg]
Case1	0.45	287	4.21×10^{-3}
Case2	0.45	301	9.83×10^{-3}
Case3	0.60	287	5.62×10^{-3}
Case4	0.60	301	1.31×10^{-2}

The supersonic nozzle geometry of computational grid is shown in Fig.1. The nozzle has a height of 44 mm at the inlet and exit, a nozzle length of 340 mm, a radius of circular arc R (characteristic length l_0)=400 mm and a height of nozzle throat 24 mm.

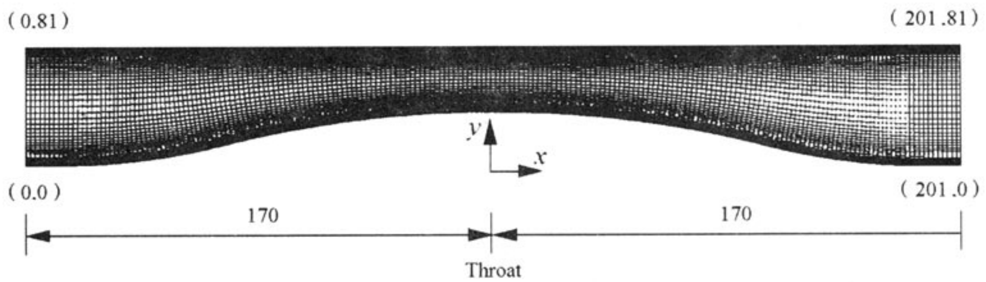

Fig.1 Computational grids

The grids contain 200 divisions in ξ-direction and 80 divisions in η-direction. The highest and lowest lines are solid boundaries and the minimum dimensional length is 3.8863×10^{-5} mm at the near wall of solid boundaries.

Inlet and exit boundaries are constrained with free boundary condition. Non-slip velocity, iso-pressure $(\partial p/\partial\eta = 0)$ and no heat transfer $(\partial T/\partial\eta = 0)$ are constrained on the nozzle wall. Condensate mass fraction $g(= m_l/(m_l+m_a))$ is set at g=0 on the wall. The value of CFL number is 0.95.

RESULTS AND DISCUSSION

Comparison with Experimental Results

Figs.2(a) and (b) show experimental results[20] for schlieren photographs and static pressure distributions, respectively, corresponding to the initial conditions as indicated in Table 1. The abscissa is the distance x from the nozzle throat divided by the characteristic length $l_0(= R)$, and on the ordinate, the local static pressure p is represented in non-dimensional form divided by the initial total pressure p_0. As seen from the pressure distributions, the simulated results are compared with experimental data in reasonable agreement.

Points A, B and C shown in Fig.2(b) denote the onset of condensation (separating point from isentrope), the end of non-equilibrium condensation (maximum value of pressure) and arbitrary location in the downstream, respectively. As will be shown later, points A and B correspond to the maximum value of local degree of supersaturation $S(= p_v/p_{\infty})$ and I_F=0, respectively. As seen from schlieren photographs, λ and normal type condensation shock waves are observed in Cases 2 and 4, respectively. Thus, it is seen that increase of the release of latent heat with an increasing ω_0 affects the flowfield largely.

Variations of Flow Properties

Fig.3 shows static pressure and frozen Mach number distributions for Case 2. Frozen Mach number distributions on the flat and curved walls denote the ones at a short distance from both walls. Points A and B denote the onset of condensation and the end of non-equilibrium condensation. As seen from this, distributions on curved wall have two maximum values due to the effect of curvature of the nozzle. This is obvious from the facts that there is a λ type shock

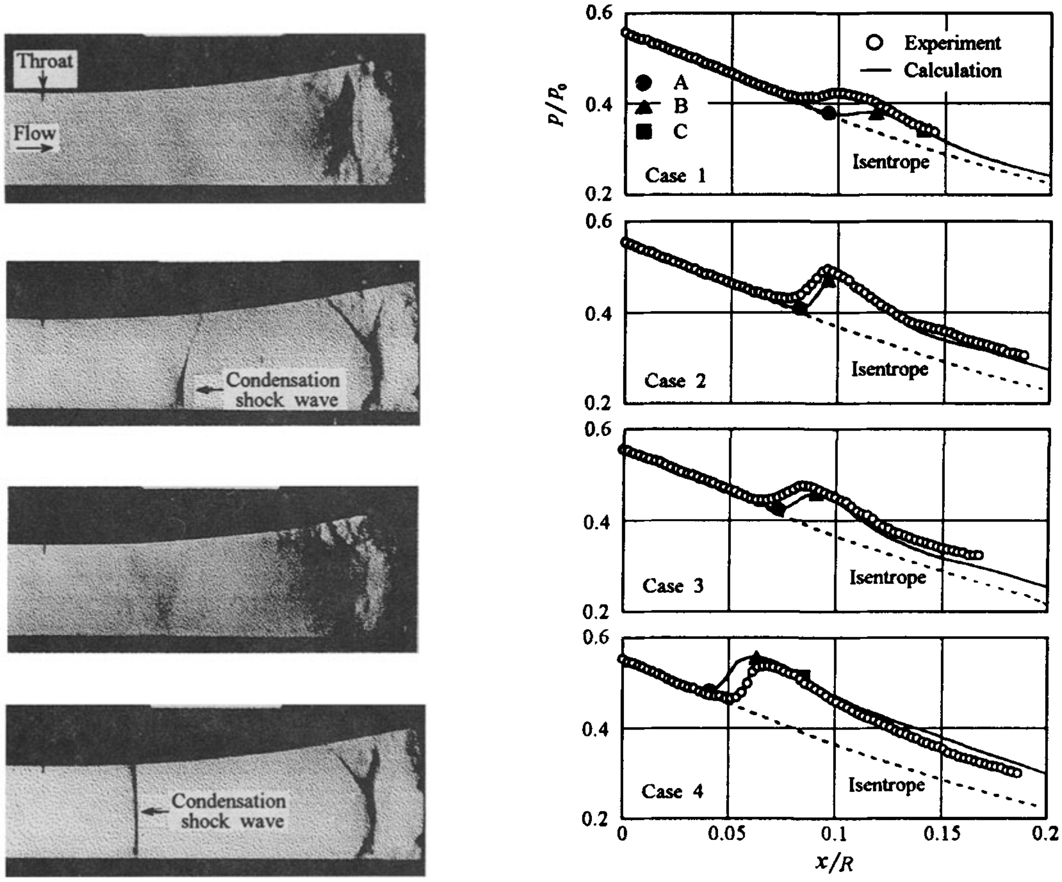

Fig.2 Schlieren photographs and pressure distributions
(a) Schlieren photographs[20] (b) Pressure distributions

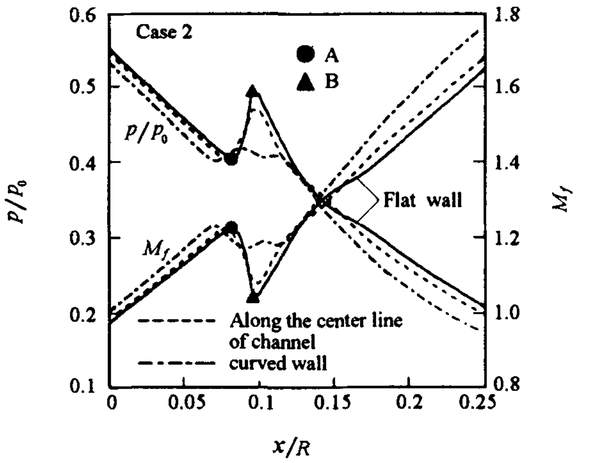

Fig.3 Pressure and Mach number distributions (Case2)

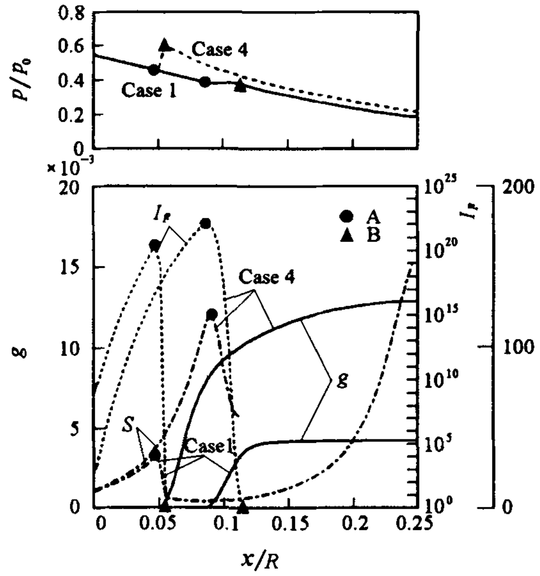

Fig.4 Variations of condensate mass fraction, nucleation rate and local degree of supersaturation on the center wall (Cases 1 and 4)

wave in the flow field as shown in Fig.2(a) and density contour map which is shown in Fig.7(b).

Fig.4 shows static pressure p/p_0, local degree of supersaturation S, condensate mass fraction g and nucleation rate I_F on the center line for Cases 1 and 4, re- spectively. As seen from this, maximum values of S and I_F are obtained at point A (onset of condensation). This point is considered to be a diverting point from isentrope. The condensate mass fraction g increases rapidly from point A and approaches the value of specific humidity ω_0 in the reservoir.

Fig.5 shows temperature T/T_0, density ρ/ρ_0 and static pressure p/p_0 distributions on the flat wall for Cases 1~4. Distributions in each case start to divert from isentrope at point A, and point A moves upstream with an increase of ω_0. From these results, it is considered that condensation affects the boundary layer largely as the release of latent heat increases with an increasing ω_0. The effect of condensation on the boundary layer will be presented in detail in Figs. 8~11.

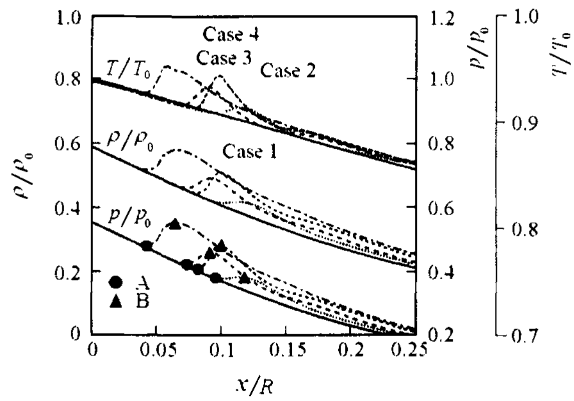

Fig.5 Temperature, density and pressure distributions along the flat wall

Contour Maps of Flow Field

Fig.6 shows contour maps of pressure, density, temperature, condensate mass fraction and nucleation rate for Case 1. The upper and lower parts indicate maps in cases with and without condensation, respectively. The values of $\Delta p, \Delta \rho$ and ΔT are indicated by dimensionless quantities to reservoir condition. As is evident from this, flowfields with condensation are largely changed in comparison with no condensation. From density and temperature contour maps, the development of boundary layer is restrained in the downstream of condensation zone (A-B) by the occurrence of condensation. As a result, it may be considered that the development of the boundary layer becomes small due to condensation. These phenomena are also described in Refs. [18,20,37]. According to Refs.[20,37], the decrease in boundary layer thickness behind condensation zone is considered to be due to the reduction of kinematic viscosity induced by increase of density.

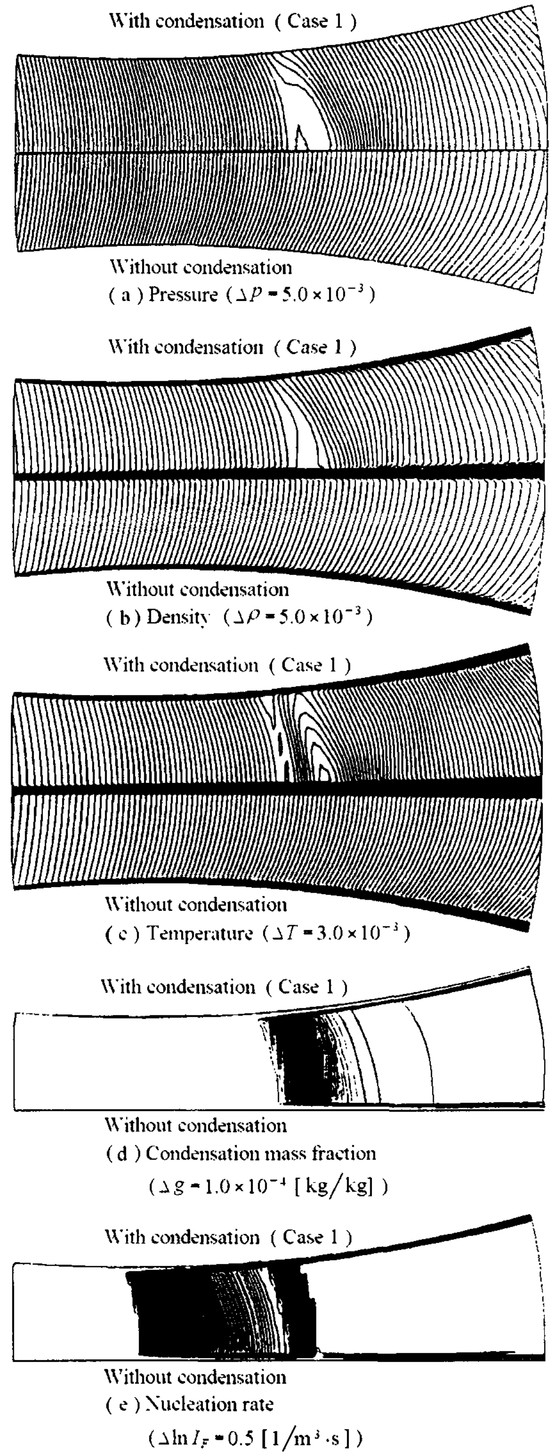

Fig.6 Contour maps of pressure, density, temperature, condensate mass fraction and nucleation rate

Condensate mass fraction g increases rapidly. Nucleation rate I_F decreases and approaches the value of zero. In the boundary layer, g and I_F do not exist and there is a large gradient of g and I_F at the edge of boundary layer.

Fig.7 shows contour maps of density in cases with condensation for Cases 1~4. Close agreement between schlieren photographs shown in Fig. 2(a) and simulated results is obtained. Furthermore, the development of boundary layer in the downstream region behind condensation zone is restrained in comparison with the case without condensation for all cases. However, for Cases 2~4, thickness of the boundary layer becomes thick in the region of condensation zone in comparison with the case without condensation. This is considered to be due to rapid increase of pressure in the region of condensation zone.

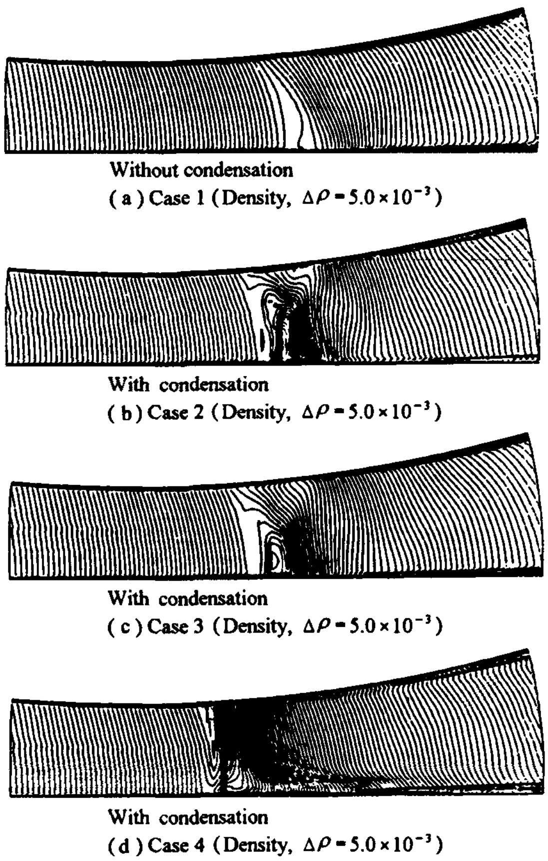

Fig.7 Density contours for Cases 1 to 4

Effect of Condensation Affecting Boundary Layer

Fig.8 shows the plots of the velocity profiles using inner-law variables y^+ and u^+ at points B and C for Case 4. y^+ and u^+ are defined as follows:

$$u^+ = \frac{u}{v_{*0}}, \quad y^+ = \frac{y v_{*0}}{\nu} \quad (v_{*0} = \sqrt{\tau_W/\rho_W})$$

In this figure, lines for the viscous sublayer ($y^+ \leq 5$) and turbulence region ($y^+ \geq 30$) are indicated for the case of turbulent flow past smooth flat wall. As seen from this, the velocity profile for no condensation (symbol •) is almost the same as that with condensation. For case with condensation, the velocity profile is only affected in turbulence region ($y^+ \geq 30$).

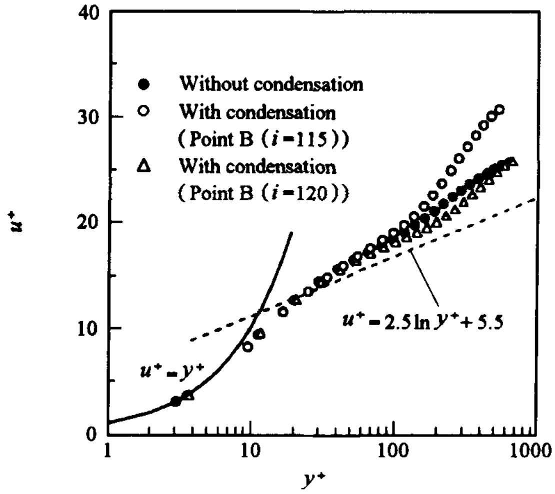

Fig.8 Velocity profiles using inner-law variables y^+ and u^+

Figs. 9(a) and (b) show distributions of skin friction coefficient (C_f) on the flat wall for Cases 1 and 4, respectively. C_f is defined as follows:

$$C_f = \frac{\tau W}{\frac{1}{2}\rho u_\infty} \tag{10}$$

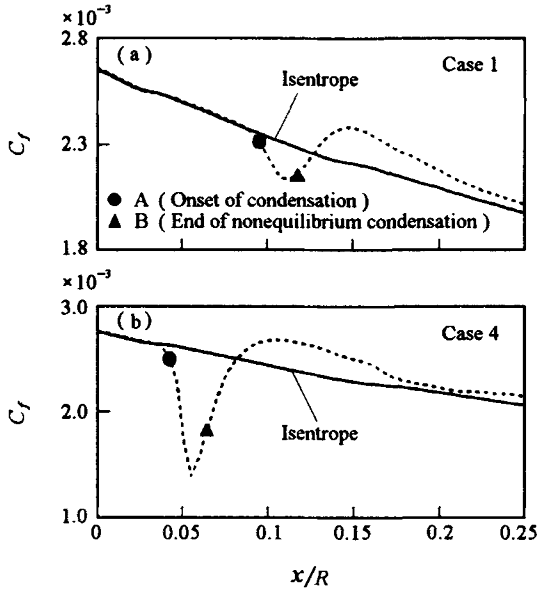

Fig.9 Skin friction coefficients on the flat wall (Cases 1 and 4)

Solid line indicates C_f distribution for the case without condensation. As is evident from both figures, values of C_f decrease from the near point of A. This is considered to be due to the effect of reduction of velocity gradient near the wall. From results described above, increase of u^+ in turbulence region at point B is due to reduction of shear stress on the wall. The characteristic of distributions for Cases 1 to 3 is almost the same as that for Case 4.

Figs.10(a) and (b) show velocity and temperature profiles to reservoir condition from the flat wall to the edge of the boundary layer at points A, B and C for Cases 1 and 4, respectively. j denotes the position of mesh point from the flat wall. Velocity profiles at points B and C are changed largely for the case with condensation and velocity gradients near the wall are reduced. Furthermore, temperature profiles are also changed largely due to the release of latent heat in main stream and especially the largest change is for Case 4.

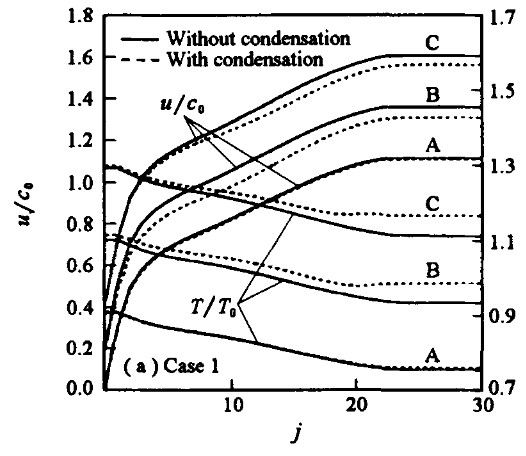

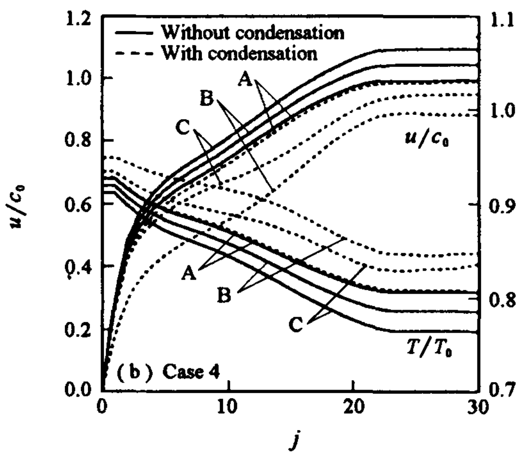

Fig.10 Velocity and temperature profiles
(a) Case 1; (b) Case 4

Fig.11 shows variations of displacement thickness δ^* on the flat wall for Cases 1 to 4. δ^* is defined as follows:

$$\delta^* = \int_0^\infty \left(1 - \frac{\rho u}{\rho_\infty u_\infty}\right) \mathrm{d}y \tag{11}$$

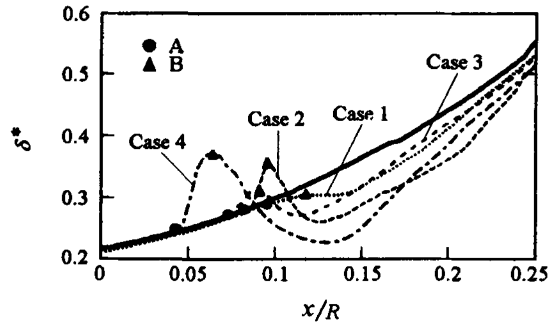

Fig.11 Boundary layer displacement thickness

Solid line indicates displacement thickness for no condensation. Diverting points from the line correspond to the onset of condensation. As seen from this figure, the displacement thickness downstream of the condensation zone becomes small for all cases. In the downstream including condensation zone for weak condensation of Case 1, δ^* decreases in comparison with no condensation. However, δ^* increases in the region of condensation zone for Cases 2 to 4. This is considered to be due to rapid increase of pressure as described in Section 6.2.

CONCLUSIONS

Numerical investigations were carried out in order to clarify the effect of condensation produced by the expansion of moist air in a supersonic half nozzle on the flowfield. The results obtained are summarized as follows:

(1) Simulated results using turbulence model, are in good agreement with experimental results, and it is clarified that the occurrence of condensation affects largely the velocity and temperature profiles in the boundary layer.

(2) Skin friction coefficient near the condensation zone decreases in comparison with no condensation. This is considered to be due to the effect of reduction of velocity gradient near the wall.

(3) Condensation affects u^+ in turbulence region of $y^+ \geq 30$. This is considered to be due to the reduction of shear stress on the wall.

(4) In the downstream including condensation zone for case with weak condensation, δ^* decreases in comparison with no condensation. On the other hand, for case with strong condensation, δ^* increases in the region of condensation zone. This is considered to be due to rapid increase of pressure.

REFERENCES

[1] Oswatitsch, K., "Kondensationserscheinungen in Ueberschallduesen," Z. angew. Math. Mech. 22, p.1., (1942).

[2] Wegener, P.P. and Mach, L.M., "Condensation in Supersonic and Hypersonic Wind Tunnels," Adv. in Appl. Mech., **5**, p.307, Academic Press, (1958).

[3] Wegener, P.P. and Pouring, A.A., "Experiments on Condensation of Water Vapour by Homogeneous Nucleation in Nozzles," *Phys. Fluid, 7,* No.3, p.352, (1964).

[4] Pouring, A. A., "Thermal Choking and Condensation in Nozzles," *Phys. Fluid,* **8,** No.10, p.1802, (1965).

[5] Zierep, J. und Lin, S., "Bestimmung des Kondensationsbeginns bei Entspannung feuchter Luft in Ueberschallduesen," Forsh. Ing. -Wes., **33,** p.169, (1967).

[6] Matsuo, K., Kawagoe, S., Setoguchi, T. and Sonoda, K., "Condensation Shock and Examples," *Machine Study, (in Japanese),* **36,** No.1, p.73, (1984).

[7] Matsuo, K. Kawagoe, S., Sonoda, K. and Sakao, K., "Study on Condensation Shock Wave," *Trans. Jpn. Soc. Mech. Eng., (in Japanese),* **50,** No.459, p.2577, (1984).

[8] Matsuo, K., Kawagoe, S., Sonoda, K., Kwon, S. B., Yamamoto, H. and Sugiyama, E., "Studies of Condensation Shocks (2nd Report, Relation between Condensation Shock and Condensation Zone)," *Trans. Jpn. Soc. Mech. Eng., (in Japanese),* **51,** No.466, p.1952, (1985).

[9] Matsuo, K., Kawagoe, S., Sonoda, K. and Sakao, T., "Study on Condensation Shock Waves (Part 1, Mechanism of their Formation)," Bull. JSME, **28,** No.241, p.1416, (1985).

[10] Matsuo, K., Kawagoe, S., Sonoda, K., Kwon, S.B., Yamamoto, H. and Sugiyama, E., 2nd Report, "Relation between Condensation Shock Wave and Condensation Zone)," *Bull. JSME,* **29,** No.248, p.439, (1986).

[11] Zierep, J., "Stroemungen mit Energiezufuhr," **2,** Aufl., G. Braun, Karlsruhe, (1990).

[12] Schnerr, G.H. and Dohrmann, U., "Transonic Flow Around Airfoils with Relaxation and Energy Supply by Homogeneous Condensation," *AIAA J.,* **28,** No.7, p.1187, (1990).

[13] Schnerr, G.H., "Homogene Kondensation in Stationaeren Transsonischen Stroemungen durch Laval-duesen und um Profile," Hab. schrift, Universitaet Karlsruhe, (1986).

[14] Ikeda, T. and Suzuki, A., "Some Findings on the Flow Behaviour of Last-Stage Turbine Buckets by Linear Cascade Tests in Steam," *Instn. Mech. Eng. Conf. Publ.,* **3,** p.46, (1973).

[15] Gyarmathy, G., "Two-Phase Flow in Turbines and Separators," edited by Moor, M.J. and Sieverding, C.H., p.127, McGraw-Hill, (1976).

[16] Nagayama, T., Kuramoto, Y. and Imaizumi, M., "The Effect of the Air Humidity on the Cascade Performance in the Suction Type Shock Tunnel," *Journal of the Japan Society for Aeronautical and Space Sciences,* **30,** No.337, p.83, (1982).

[17] Kwon, S.B., Matsuo, K., Kawagoe, S., Setoguchi, T., Noda, S. and Matsuo, S., "Effects of Condensing Flow on an Oblique Shock Wave in a Supersonic Nozzle," *Trans. Jpn. Soc. Mech. Eng.,* (in Japanese), **54,** No.500, p.798, (1988).

[18] Schnerr, G., Bohning, H.R., Breitling, T. and Jantzen, H.-A., "Compressible Turbulent Boundary Layers with Heat Addition by Homogeneous Condensation," *AIAA J.,* **30,** No.5, p.1284, (1992).

[19] Iriya, A., Yamamoto, S. and Daiguji, H., "Numerical Method for Transonic Viscous Flow Considering Humidity (in Japanese)," *Trans. Jpn. Soc. Mech. Eng., (in Japanese),* **62,** No.603, p.3854, (1996).

[20] Setoguchi, T., Matsuo, S., Yu, S. and Hirahara, H., "Effect of Nonequillibrium Homogeneous Condensation on Flow Fields in a Supersonic Nozzle," *Journal of Thermal Science,* **6,** No.2, p.90, (1997).

[21] Baldwin, B.S. and Lomax, H., "Thin Layer Approximation and Algebraic Model for Separated Turbulent Flows," AIAA Paper 78-257, (1978).

[22] Gyarmathy, G., Forsch. Ing. Wes., Bd.29, p.105, (1963).

[23] Vincenti, W.G. and Kruger, C.H., Introduction to Physics Gas Dynamics, p.254, Robert E. Krieger Publishing Company, (1969).

[24] Wegener, P.P, Nonequilibrium Flow, Part 1, p.163, Marcel Dekker, (1969).

[25] Sislian, J.P., "Condensation of Water Vapor with or without a Carrier Gas in a Shock Tube," UTIAS Rep., 201, (1975).

[26] Abraham, F.F., ≪Homogeneous Nucleation Theory≫, Academic Press, (1974).

[27] Wegener, P.P. and Wu, B., ≪Nucleation Phenomena≫, edited by Zettlemoyer, A.C., p.325, ELSEVIER, (1977).

[28] Mills, A.F. and Seban, R.A., *Int. J. Heat Mass Transf.,* **10,** p.1815, (1967).

[29] Pound, G.M., J. Phys. Chem. Ref. Data, **1,** No.1, p.119, (1972).

[30] Watanabe, K., Yata, J. and Minamiyama, T., *Jour. Jpn. Soc. Mech. Eng., (in Japanese),* **81,** p.1182, (1978).

[31] Kawata, H. and Mori, Y., *Trans. Jpn. Soc. Mech. Eng, (in Japanese),* **38,** No.35, p.2843, (1972).

[32] Kirkwood, J.G. and Buff, F.P., *J. Chem. Phys.,* **17,** p.3389, (1949).

[33] Oriani, R.A. and Sundquist, B.E., *J. Chem. Phys.,* **38,** p.2082, (1963).

[34] Yee, H.C, "A Class of High-Resolution Explicit and Implicit Shock-Capturing Methods," NASA TM 89464, (1989).

[35] Pulliam, T.H. and Chaussee, D.S., "A Diagonal Form of an Implicit Approximate-Factorization Algorithm," *J. Comp. Phys.,* **39,** p.347, (1981).

[36] Kwon, S.B., Matsuo, K., Kawagoe and Matsuo, S., "Total Pressure Loss in Supersonic Nozzle Flows with Condensation (Numerical Analyses)," *JSME International Journal, Series 2,* **31,** No.1, p.16, (1988).

[37] Hirahara, H., Yamashita, K., Kawahashi, M. and Wu, L.Y., "Numerical Simulation of Compressible Viscous Two-Phase Flow with Condensation," *Trans. Jpn. Soc. Mech. Eng., (in Japanese),* **61,** No.582, B, p.399, (1995).